Titre: Title:	Micro-infiltration of three-dimensional porous networks with carbon nanotube-based nanocomposite for material design
Auteurs: Authors:	Rouhollah Dermanaki Farahani, Hamid Dalir, Brahim Aïssa, My Ali El Khakani, Martin Lévesque, & Daniel Therriault
Date:	2011
Type:	Article de revue / Article
Référence: Citation:	Farahani, R. D., Dalir, H., Aïssa, B., El Khakani, M. A., Lévesque, M., & Therriault, D. (2011). Micro-infiltration of three-dimensional porous networks with carbon nanotube-based nanocomposite for material design. Composites Part A: Applied Science and Manufacturing, 42(12), 1910-1919. https://doi.org/10.1016/j.compositesa.2011.08.016

0 L F U R L Q I L O W U D W L RQQD R I SWRKURHKHV GQLHPWHZQRVULNRV Z L W
Q D Q R W X E H E D V HLGWQ DIQR RUFRDPSWRVU L D O G H V L J

Rouhollah D. Farahani[a], Hamid Dalir[a], Brahim Aissa[b], My Ali El Khakani[b], Martin Lévesque[a], and Daniel Therriault[a]*

[a] Center for Applied Research on Polymers and Composites (CREPEC), Mechanical Engineering Department, École Polytechnique de Montréal, C.P. 6079, Succ. Centre-Ville, Montreal (QC), Canada H3C 3A7
[b] Institut National de la Recherche Scientifique, INRS-Énergie, Matériaux et Télécommunications, 1650 Blvd. Lionel-Boulet, Varennes (QC), Canada J3X 1S2

* Corresponding author:
Phone: 1-514-340-4711 x4419
Fax: 1-514-340-4176
E-mail: daniel.therriault@polymtl.ca

$ E V W U D F W

Epoxy composite beams reinforced with a complex three-dimensional (3D) skeleton structure of nanocomposite microfibers were fabricated via micro-infiltration of 3D porous microfluidic networks with carbon nanotube nanocomposites. The effectiveness of this manufacturing approach to design composites microstructures was systematically studied by using different epoxy resins. The temperature-dependent mechanical properties of these multifunctional beams showed different features which cannot be obtained for those of their individual components bulks. The microfibers 3D pattern was adapted to offer better performance under flexural solicitation by repositioning most of the reinforcing microfibers at higher stress regions. This led to an increase of 49% in flexural modulus of a reinforced-epoxy beam in comparison to that of the epoxy bulk. The flexibility of this

method enables the utilization of different thermosetting materials and nanofillers in order to design multifunctional composites for a wide variety of applications such as structural composites and components for micro electromechanical systems.

. H \ Z R UAG T Thermosetting resin, B. Mechanical properties, B. Microstructures, E. Assembly, nanocomposite.

, Q W U R G X F W L R Q

Micro- and nano-fibers have been increasingly used as reinforcement in epoxy-based composites for structural applications in aerospace [1,2] and organic electronics [3]. Since epoxies are known to exhibit low toughness and impact resistance, several approaches have been employed to improve specific properties of fiber-reinforced epoxies [4]. Among these approaches, the selection of suitable reinforcement which optimizes the composite properties [5], the improvement of the matrix toughness with other thermosetting resins or thermoplastics [6], and the critical optimization of the fiber-matrix interface to enhance the stress transfer properties [4] can be cited. Recently, multiscale approaches have been developed to design optimized microstructures using both nanoscale and microscale reinforcements [7].

Fibers produced from polymers such as polypropylene and nylon have been recently used as reinforcements for the fabrication of polymeric composites [8]. Various fiber parameters such as material nature, aspect ratio, fibers alignment, volume fraction, processing technique and fiber-matrix interface have been shown to influence the general performance of such composites. Main challenges with these polymeric fibers are their

adhesion to the epoxy matrix and their lower mechanical properties with respect to traditional fibers [8,9]. However, fabrication of nanocomposite microfibers by the addition of nano-particles having superior mechanical properties could further enhance the effectiveness of the polymeric fibers, which could lead to physical and mechanical properties improvement in these types of multiscale composites. Single-walled carbon nanotubes (SWCNTs) have been identified to be highly promising candidates for reinforcing polymer fibers not only for enhancing mechanical properties of the resulting nanocomposite [10-13], but also for improving their electrical [10,14] and thermal [15] properties, even for very low loadings. Hence, specific properties of an epoxy matrix could be tailored by taking the advantages of other polymers as fibers combined with excellent properties of SWCNTs. For specific loading conditions, positioning the nanocomposite microfibers at higher stress regions in these multifunctional composites could enhance their effectiveness compared to nanocomposites with randomly distributed fibers.

In this paper, we report on the use of a composite manufacturing approach inspired from an original microfluidic infiltration technique which was recently developed in our laboratory [16]. This approach is based on the micro-infiltration of a 3D microfluidic network with SWCNTs-based nanocomposite suspension for the fabrication of 3D-reinforced multiscale composites. After micro-infiltrating, the nanocomposite suspension was cured, resulting in a multiscale composite which consists of a complex 3D skeleton structure of nanocomposite microfibers. The micro-infiltration technique enables orienting the nanotubes along the fiber axis [17] and thus positioning the nanocomposite fibers into a designed pattern for optimal conditions. Hence, the most of nanocomposite microfibers were positioned at higher stress regions to offer better performance under flexural solicitation.

Another focus is put here on the comparative study of three different epoxy resins with different properties (i.e., mechanical properties and glass transition temperatures) in order to point out the respective influences of both matrix and nanocomposite fibers on the overall properties of resulting reinforced beams. The temperature-dependent mechanical and flexural properties of the fabricated multiscale nanocomposites were characterized with dynamic mechanical analyzer (DMA) and quasi-static three-point bending tests, respectively. These properties of the 3D-reinforced beams showed different features which usually cannot be obtained in their components bulks. The performance of the nanocomposite and 3D-reinforced beams were also characterized under tensile testing. The results provide sufficient evidence that the applied loads are effectively transferred to the 3D-patterned fibers (microscale) and subsequently to the SWCNTs in the nanocomposite-based fibers (nanoscale). The present manufacturing method opens new prospects for the design of multifunctional composite materials for optimal conditions.

2. Experimental

2.1. Nanocomposite preparation

The SWCNTs were produced by means of the pulsed laser ablation technique, using an excimer KrF laser (248 nm, 20 ns, 50 Hz, 300 mJ). The as-grown SWCNTs were chemically purified and functionalized by refluxing them in a 3M-HNO_3 (Sigma-Aldrich) solution for 5h (More details on the SWCNTs growth and purification can be found elsewhere [18]). The nanocomposites were prepared by blending purified-SWCNTs (at two loads of 0.5wt% and 1wt%), as reinforcement, and two different epoxy resins, either a special one-component dual cure (ultraviolet/heat curable) epoxy resin (UV-epoxy, UVE,

UV15DC80, Master Bond Inc.) or two-component epoxy (EPON 862/ANCAMINE 2049), as matrices. The purified-SWCNTs were first dispersed in a solution of 0.1 mM of protoporphyrin IX (PP, Sigma-Aldrich) in acetone (Sigma-Aldrich) by bath ultrasonication (Ultrasonic cleaner 8891, Cole-Parmer) for 30 min. The resins were then mixed with the nanotube suspension in acetone overnight using a magnetic stirring hot plate (model SP131825, Barnstead international) at 50°C for 4 h. The residual solvents were evaporated by heating the mixtures at 30°C for 12 h and at 50°C for 24 h in a vacuumed-oven (Cole Parmer). After evaporation of solvent, the nanocomposites were subjected to high shear mixing through a very small gap in a three-roll mill mixer (Exakt 80E, Exakt Technologies) for several times in progressing steps [19]. The gap between rolls were adjusted at 25 µm for 5 passes and 10 µm for another 5 passes, followed by 10 passes at 5 µm while the speed of apron roll was 250 RPM. The final mixtures were then degassed under vacuum of 0.15 bar for 24 h. For the mixture prepared with the EPON 862 resin, the curing agent (resin:curing agent weight proportion = 3:1) was then mixed with the nanocomposite mixture and was passed in the three-roll mill mixer for 5 times with a gap of 15 µm and an speed of 250 RPM. The final mixture was degassed under vacuum of 0.15 bar for 2 h.

) D E U L F D W L R Q R I ' P L F U R I O X L G L F Q H W Z R U N V

Three-dimensional microfluidic networks were fabricated via the robotic deposition of a fugitive organic ink scaffold structure [20,21]. The fugitive ink was a 40 wt% binary mixture of a microcrystalline wax (SP18, Strahl & Pitsch) and a petroleum jelly (Lever Pond's). Figure 1(a) schematically illustrates the ink deposition process. The fabrication of the scaffold began with the deposition of the ink-based filaments on an epoxy substrate

using a computer-controlled robot (I & J 2200-4, I & J Fisnar) and a dispensing apparatus (HP-7X, EFD), leading to a two-dimensional pattern. The following layers were deposited by successively incrementing the deposition of the dispensing nozzle by the diameter of the filaments. The filaments' diameter was 150 μm for a deposition speed of 4.7 mm/s at an extrusion pressure of 1.9 MPa. The overall dimensions of the 3D ink structure were 62 mm in length, 8 mm in width and 1.7 mm in thickness. The scaffold consisted of eleven layers of fugitive ink filaments, in which each layer was alternatively oriented along and perpendicular to the scaffold longitudinal axis. The number of filaments deposited along the width direction, n_x (even layers) was constant while the number of filaments along the longitudinal direction (odd layers, n_y) gradually decreased from the outer layers (1 and 11) to the center of structure in middle layers (5 and 7). Considering that the fugitive ink will be eventually replaced by the infiltrated-nanocomposite fibers, the reinforcing pattern can be tailored at will by using the flexible direct-write assembly method. In other words, depending on the final application of the microstructure, quantity and position of the reinforced filaments can be easily controlled for optimal properties. Axial stress distribution linearly increases from the neutral mid-plane to a maximum value at the outer surfaces during flexural mechanical solicitation. Thus, the number of axial reinforcing infiltrated microfibers was increased in higher stress regions to offer optimal performance under flexural solicitation.

After the deposition, the ink-based scaffolds were surrounded with two different epoxy resins: either EP1 (Epon 828/Epikure 3274, Miller-Stephenson Chemical Co.) or EP2 (Epon862/Ancamine 2049, Miller-Stephenson Chem. Co./Air Products Inc.), as shown in Figure 1(b). Prior to encapsulation, the epoxy systems were degassed under

vacuum of 0.15 bar for 1 h to remove the bubbles trapped during mixing the epoxy components. For epoxy encapsulation, drops of epoxy were placed over the inclined (30°) scaffold structure at its upper end and let the epoxy to flow into the pore spaces between filaments through gravity and capillary forces. The quantity of the epoxy was controlled using a fine needle (7018225, EFD, internal diameter = 0.51mm) connected to a fluid dispenser (EFD800, EFD) in order to minimize the risk of bubble trapping [22-24]. When the epoxy resin reached the lower end of the scaffold, the resin-encapsulated structure was placed under a vacuum of 0.4 bar for eliminating the remaining bubbles. The low viscosity of the epoxy system prior its full curing enhanced the degassing effect. The fiber displacement might be another issue that affects the encapsulation process. The rigidity of the fugitive ink used in this study enables both the scaffolds to retain their shape during the fabrication and subsequent epoxy encapsulation under ambient conditions [20]. After the pre-curing of the surrounding epoxy resin at room temperature for 48 h, the ink was removed by liquefaction at ~100°C in a vacuumed-oven for 30 min, as shown in Figure 1(c). Shortly after taking the samples out of the oven, the channel networks were washed with the suction of boiling distilled water for 5 min followed by hexane (Sigma Aldrich) for another 5 min.

3 U H S D U D W L R Q R I U H V L Q L Q I L O W U D W H G ' E H D P V Y L Y O L W D U L D W L R Q W H F K Q L T X

The 3D-reinforced beams were produced by micro-infiltrating the created tubular microfluidic networks with the pure epoxy resin (defined as resin-infiltrated beams) and their nanocomposites counterparts (defined as nanocomposite-infiltrated beams). The materials infiltrated behave like microscale fibers inside an epoxy matrix. Figure 1(d)

schematically illustrates the micro-infiltration step for a nanocomposite-infiltrated beam at both micro- and nanoscales. The empty channels were infiltrated by the pure epoxy resins and their nanocomposites using the fluid dispenser via a plastic tube connected to the end of the beams and the fluid dispenser at both ends. The infiltration pressure was adjusted at 400 kPa, which led to an average infiltration speed of ~1 mm/s. In resin transfer molding (RTM) process, two major issues may arise when a liquid resin with nanoparticles is injected into the mold containing fibrous performs; void formation and nanoparticle deposition [23,25-28]. As in vacuum assisted resin transfer molding (VARTM) [29], a vacuum of 0.3 bar was applied to the other end (i.e. outlet side) of the microfluidic network in order to reduce the formation of voids. This not only contributed to provide the required pressure gradient for the infiltration of the nanocomposite, but also made less air available at the flow front to be entrapped [22]. The bubbles created during the infiltration process were moved with the material flow and gradually escaped by keeping the applied pressure for 30 sec after complete filling of the channels. Few holes were drilled in the length-thickness plane of the beams (each 20 mm on sides) in order to remove the bubbles that might still existed in the width-channels as possible stationary points. Shortly after, the infiltration process was resumed for another 30 sec. Second, deposition of nanofillers potentially leading to a total blockage of the flow has been reported for RTM and VARTM processes [27,28,30]. This issue is of importance when large clusters are passed through smaller channels. Considering the size of SWCNT aggregates in our study (~2 µm max.), it is thought that their deposition inside the channels of ~ 160 µm is unlikely. Other nanoparticle deposition mechanisms, like sedimentation of nanoparticles due to their gravity and non-Newtonian behavior, have also been reported [27]. Since the SWCNTs and

the epoxies used in this study had similar densities, sedimentation of nanoparticles might be negligible. The effect of Non-Newtonian behavior is also unlikely since Newtonian behavior or slight shear thinning of the nanocomposites were observed (results for rheological behavior are not shown here).

After micro-infiltration step, the beams filled by the UV-epoxy- and its associated nanocomposite were put under illumination of a UV lamp with an intensity of 21mW/cm² (Cole-Parmer) for 30 min for pre-curing. The beams were then post-cured in the oven at 80 °C for 1 h followed by 130°C for another 1 h. The cure schedule for the second type of beams that were filled by EPON 862 resin and its associated nanocomposites was 90 °C for 2 h followed by 130°C for another 2 h. All the beams were cut and polished to the desired dimensions (i.e., ~60 mm in length, ~7.5 mm width and ~1.7 mm in thickness). Figures 2(a) and 2(b) show an isometric and cross-sectional view of a nanocomposite-infiltrated beam, respectively. To verify presence of trapped bubbles, the cross-sections of few representative beams were observed under optical microscope for different locations along both longitudinal and width directions. No voids were seen, indicating the proper filling of the microfluidic channels. This also suggests that the filling speed did not affect the infiltration process since it reduces gradually towards the other end of the beams. Figures 2(c)-(e) show schematics of the cross-section of porous, resin-infiltrated and nanocomposite-infiltrated beams, respectively. Table 1 lists the different types of beams manufactured along with their components. For each type of beams, nine samples were prepared for mechanical testing. Three bulk specimens (molded samples) for each epoxy (i.e., EP1, EP2 and UVE) having the same dimensions as the beams were also prepared for comparison purposes.

0RUSKRORJLFDO DQG PHFKDQLFDO FKDUDFWHUL]DWLI

The purified SWCNTs were observed by transmission electron microscopy (TEM) using a Jeol JEM-2100F (FEG-TEM, 200 kV) microscope in order to characterize the nanotube structure. Raman spectra were acquired at room temperature in the 100-2000 cm^{-1} spectral region under ambient conditions using a back-scattering geometry on a microRaman spectrometer (Renishaw Imaging microscope Wire TM) with a 50× objective to focus the laser beam on the sample. The sample excitation was performed by using a 514.5 nm (2.41 eV) line from an air cooled Ar+ laser.

For optical imaging purposes, a ~20 μm-thick film of the nanocomposite was fabricated via its direct deposition on a glass substrate by means of the pressure dispensing-equipped robot. The quality of the mixing was observed for the cured nanocomposite film using an optical microscope (BX-61, Olympus) and image analysis software (Image-Pro Plus6, Media Cybernetics). Gold-coated fracture surfaces of the resin-infiltrated and the nanocomposite-infiltrated beams were observed using field emission scanning electron microscopy (FESEM) (JEOL, JEM-2100F) at 2 kV in order to observe the failure mode.

Temperature-dependent mechanical properties (complex modulus, $E^* = E' + iE''$, where E' is the storage modulus and E'' is the loss modulus) of the beams were measured in a DMA (DMA 2980, TA instruments) with a three-point bending mode at a ramp rate of 3°C/min and at a frequency of 1 Hz over the temperature range of 25 - 160°C. Quasi-static three-point bending tests were conducted on a DMA (DMA 450, 01 DB-MetraviB) with a maximum load of 450 N and a crosshead speed of 0.5 mm/min for a support span of 35 mm according to the standard ASTM D790. Tensile properties (i.e., tensile modulus and

strength) of the reinforced beams were also measured in a tensile testing machine (Instron 4400R) with a load cell of 5 kN according to the ASTM D638 standard. The crosshead speed was set to 1 mm/min. Typical dimensions of the infiltrated- and bulk-beams were 60 mm × 7.5 mm × 1.7 mm.

5HVXOWV DQG GLVFXVVLRQ

&DUERQ QDQRWXEH FKDUDFWHUL]DWLRQ

Figure 3(a) shows typical TEM micrographs of the laser-synthesized SWCNTs after their purification and functionalization. The nanotubes are seen to self-organize into bundles of few nanotubes and occasionally individual SWCNTs. These SWCNTs feature a high aspect ratio since their length can reach up to several microns and their diameter is in the nanometer range. The inset of Figure 3(a) shows a bundle of SWCNTs where a carbon nanotube with a diameter of ~1.2 nm is clearly distinguished. Structural information on the diameter of nanotubes in a given sample can be directly obtained by analyzing Raman spectra, particularly in the low frequency region where the radial breathing mode (RBM) bands occur. Figure 3(b) shows a typical spectrum of the purified SWCNTs with a narrow radial breathing mode (RBM) band centered around 185 cm^{-1}. The frequency positions of the RBM vibrational mode can be used to determine the nanotubes diameters by means of the relationship reported by Bandow *et al.* [31]:

$$\omega_{RBM}\,(cm^{-1}) = 223.75 / (d_t\,(nm)) + 12.5 \qquad (1)$$

where G and are the diameter of nanotubes and the frequency of the RBM vibrational mode. According to the equation (1), our SWCNTs are found to have a narrow diameter distribution centered around 1.2 nm, in accordance with the direct measurement of TEM (inset of Figure 3(a)).

0 R U S K R O R J L F D O F K D U D F W H U L] D W L R Q

Figure 4 shows an optical micrograph of a representative UVE nanocomposite film with 0.5 wt% of nanotube. The observed dark spots are thought to be nanotubes aggregates, the majority of which has a size in the sub-micron range (Although some micron-size aggregates of up to ~1 m-diam. are also present). The fairly uniform dispersion of the nanotube aggregates might be attributed to the effectiveness of the nanocomposite mixing procedure combining ultrasonication and three-roll mill mixing and also the presence of chemical groups at nanotube-matrix interface [32]. The chemical groups were grafted to the SWCNTs surfaces either in the nanotube purification process as confirmed by the X-ray photoelectron spectroscopy (XPS) results (these results can be found elsewhere [16]) or by non-covalent functionalization of the nanotubes with protoporphyrin IX as surfactant [33].

To examine the matrix-fiber interface and the composite structure, the fracture surface of two representative (one resin-infiltrated and one nanocomposite-infiltrated) beams broken during a three-point bending test were observed under SEM. Figure 5(a) and 5(c) show typical SEM images of the fracture surface of the EP2-beam/UVE-infiltrated and the EP2-beam/UVE-NC-infiltrated, respectively. No debonding and no pull-out of the embedded microfibers are observed, suggesting that the fibers were strongly adhered by the

surrounding EP2 matrix at fiber-matrix interface. This confirms the effectiveness of the cleaning procedure used for the complete removal of the sacrificial ink during the microfluidic network fabrication.

Figures 5(b) and 5(d) are close-up view of the fracture surface of the UVE- and NC-UVE-microfibers, respectively. Comparison of these fracture surfaces allows to gain insights in the different fracture mechanisms and to eventually point out the effect of the SWCNTs on the failure behavior of the microfibers. The fracture surface of the UVE-fiber is relatively smooth compared to that of NC-UVE-fiber which is seen to contain more layered features. The larger roughness of the fracture surface of the NC-UVE-fiber is thought to be due to possible toughening effect induced by the presence of carbon nanotubes as reported in literature [34].

0 H F K D Q L F D O F K D U D F W H U L] D W L R Q V

7 H P S H U D W X U H G H S H Q G H Q W P H F K D Q L F D O S U R S H U W L H V

Figure 6 shows the storage modulus (E'), and the loss modulus (E''), of the 3D-reinforced beams and the molded bulk epoxy samples. The T_g of the bulk-epoxies which is observed as a peak in the E'' curves (Figures 6(b), (d) and (f)), were measured as ~ 60°C, ~ 125°C and ~ 115°C for the bulk-EP1, bulk-EP2 and bulk-UVE, respectively. The E' and the E'' curves of the resin- and nanocomposite-infiltrated beams, in all cases, show a combination of the bulk properties of their components. For the EP1-beam/UVE-infiltrated (Figure 6(a)), a major drop of the storage modulus is observed at ~ 65°C which is near the T_g of EP1 followed by a less pronounced decrease between 80°C to 115°C, close to the T_g

of the UVE. Similar mechanism is observed for the EP1 beams filled by EP2 resin and its nanocomposite (Figure 6(e) and (f)). For the beams with EP1 as surrounding matrix (i.e., EP1-beam/UVE-infiltrated and EP1-beam/EP2-infiltrated), above 60°C, the T_g of EP1, the E' is completely controlled by the fibers, where the E' of the bulk-EP1 approaches to zero. The EP2-beam/UVE- and NC-UVE-infiltrated beams storage modulus exhibit a constant decreasing trend until a temperature of ~110°C (near the T_g of the UVE), followed by a slower decrease between 110°C to 512 °C (the latter temperature is the T_g of the EP2). Based on Figure 6, the E' of the 3D-reinforced beams are influenced by the properties of the microfibers and the surrounding matrices for the range of temperature studied, depending on the T_g of their components. In other words, the temperature-dependent mechanical properties of the epoxy matrices could be tailored by the presence of the microfibers, prepared by the other epoxy resins. Hence, 3D co-patterning of thermosetting polymers like epoxies led to make the whole epoxy composite materials with different temperature-dependent feature which usually cannot be obtained in a single material.

Table 2 summarizes the measured values of T_g and the E' of the 3D-reinforced beams and the bulk epoxies at 25°C. The variation of the E' of nanocomposite-infiltrated beams from their corresponding neat epoxy-infiltrated beams (i.e., the effect of SWCNTs addition) is presented in the last column. At 25°C, the E' of the bulk-EP1 and the bulk-EP2 are 2.95 GPa and 3.05 GPa, which are almost that of bulk-UVE. Regardless of the type of surrounding epoxies, the nanocomposite-infiltrated beams (i.e., multiscale composite beams) demonstrated a reasonable increase (above average) compared to those reported in literature as listed in Table 3) in the E' compared to the resin-infiltrated beams.

At 25°C, the (of the EP1-beam/UVE-infiltrated was measured 2.51 GPa and is found to increase to 2.91 GPa (about 16% of improvement) with the addition of nanotubes for the EP1-beam/NC-infiltrated. For the EP2-beam/NC-UVE-infiltrated, the (showed an increase of 18% compared to EP2-beam/UVE-infiltrated. The EP1-beam/NC-EP2-infiltrated resulted in a (as 3.46 GPa, about a 16% increase in comparison to the EP1-beam/EP2-infiltrated. Interestingly, the presence of SWCNTs was found to have a more pronounced enhancement effect (higher (values), particularly in the high temperature range where the UVE resin is softer. This is thought to be due to SWCNTs fair dispersion and adhesion with the matrix. At temperatures above T_g, the stiffening effect would be maximized when the well-bonded nanotubes are mobilized by the epoxy molecules [36]. Given the very low amount of SWCNT added (estimated to be ~ 0.18wt% in the whole beam), the considerable improvements of the (over the whole range of temperatures and for all the nanocomposite-infiltrated beams, suggests an extremely efficient load transfer in the 3D-reinforced beams. This stems from the fair dispersion and adhesion of our SWCNTs with the UVE matrix.

4 X D V L V W D W L F W K U H H S R L Q W E H Q G L Q J

Quasi-static three-point bending tests were performed to evaluate the effect of the microfibers and SWCNTs positioning on the mechanical properties of the 3D-reinforced beams. Figure 7 shows the averaged flexural stress-flexural strain curves in the quasi-static three-point bending tests, performed on three specimens for each beam type. The flexural

modulus, (E_f) and flexural strength, (σ_f), were calculated from the load-deflection curves according to the ASTM D790 standard for flexural testing [37].

Table 4 lists the (E_f) and the (σ_f) of the bulk epoxies, the EP2-beam/UVE-infiltrated, EP2-beam/NC-UVE-infiltrated, EP1-beam/EP2-infiltrated and EP1-beam/NC-EP2-infiltrated and also the increase of the properties of neat epoxy-infiltrated beams when SWCNTs added. The (E_f) of the bulk-EP1 and bulk-EP2 are almost twice the value of the UVE. The addition of SWCNTs in EP2-beam/NC-UVE-infiltrated led to an increase of flexural properties of the EP2-beam/UVE-infiltrated. The EP2-beam/NC-UVE-infiltrated with 0.5wt% SWCNTs in microfibers (i.e., 0.18wt% in the whole beam) showed an increase of 27% for the (E_f) and an increase of 18% for the (σ_f) when compared to the EP2-beam/UVE-infiltrated. Further improvement is achieved for EP2-beam/NC-UVE-infiltrated with 1wt% SWCNTs (i.e., 0.33wt% in the whole beam) (39% increase in modulus and 31% increase in strength). For the EP1-beam/EP2-infiltrated, the average flexural properties slightly increased when compared to the bulk-EP1 due to higher value of the material (EP2) used for the infiltration. The addition of 0.5wt% SWCNTs improved the (E_f) and the (σ_f) of the EP1-beam/NC-EP2-infiltrated by 22% and 16%, respectively. An increase of 34% in (E_f) is observed for the EP1-beam/NC-EP2-infiltrated with 1wt% SWCNTs compared to the EP1-beam/EP2-infiltrated while their (σ_f) showed an increase of 28%. Considering the very low fraction of the SWCNTs loading (i.e., 0.18wt% and 0.33wt%), these improvements in flexural properties are among the largest improvements reported so far [38].

Contrary to typical nanocomposite manufacturing methods by which the reinforcements are randomly distributed throughout the matrix, the 3D-patterning of the microfibers in the 3D-reinforced beams enabled positioning the microfibers and SWCNTs at higher stress region to offer optimal performance under flexural solicitation. The interface is more solicited during the quasi-static three-point bending test when compared to the small deformation in dynamic mechanical analyzing test. Therefore, higher flexural strain for the 3D-reinforced beams compared to those of the bulk-EP1 and the bulk-EP2 and strong bonding at the interface of the fiber and surrounding matrices suggest a proper load transfer at their interface (microscale), as observed by SEM images. The reasonable improvement of flexural properties for the NC-infiltrated beams compared to the resin-infiltrated beams might be attributed to subsequent stress transfer to the SWCNTs at nanotube/UV-epoxy interface (nanoscale) in the fibers and also to the positioning the nanotubes at higher stress regions.

7 H Q V L O H W H V W L Q J

The influence of SWCNTs on mechanical properties of the 3D-reinforced beams was also studied under tensile loadings. Table 5 lists the results obtained for the 3D-reinforced beams and the bulk epoxies. The second and third columns present the increase of properties of neat epoxy-infiltrated beams by adding SWCNTs. The incorporation of SWCNTs into the reinforced beams led to increase of Young's modulus and strength when compared to values for resin-infiltrated beams. Comparing the Young's modulus results with rules of mixtures predictions (see Table 5) showed that the SWCNTs reinforcement is close to its theoretical potential. For the calculations, the Young's modulus

of the nanotube bundles was assumed to be 220 GPa [39] and the volume fractions of 0.18 and 0.33 since the densities of SWCNT and the epoxies used were similar. The volume fraction of the nanocomposites in the whole beam was 35%. It is worth noting that the elastic modulus of the reinforced beams could be maximized by aligning SWCNTs inside the channels along the longitudinal direction [17,40]. The orientation state of SWCNTs in these multiscale composites could be controlled by considering the channels size-dependent mechanisms governing nanotube orientation. For example, applying higher pressure gradient will cause the SWCNTs to align with the flow and frequently rotate by 180° in Jeffery orbits. The Brownian motion that may impose small disturbances can contribute to the rotational motion by increasing the frequency of Jeffery orbits [27]. The experimental and theoretical studies on nanotube orientation inside the channels and its effect on mechanical properties of the final product will be presented in another paper.

& R Q F O X V L R Q

A method based on polymer micro-infiltration of a microfluidic network was used for the fabrication of multifunctional 3D-reinforced composite beams with a designed pattern of reinforcement. The temperature-dependent mechanical and flexural properties of the 3D-reinforced beams showed different features depending on the individual properties of the microfibers and surrounding epoxies. Higher mechanical properties were achieved by the incorporation of SWCNTs to the 3D microstructured beams even at a very low nanotube nominal load of 0.5wt% (0.18wt% in whole beam). The improvement of mechanical properties and SEM observations at fiber-matrix interface indicated that the load has

been effectively transferred to the fibers (microscale) and subsequently to the SWCNTs in the nanocomposite-based fibers (nanoscale). This new fabrication method may enable also to align SWCNTs in the 3D microfluidic network by using a higher filtration speed under shear flow. Due to the flexibility of this manufacturing method, various thermosetting polymer and their nanocomposites reinforced by other nanofillers such as nanoclay and nanosilver (in a wide range of viscosities) could be used either as microfibers or as a host matrix, depending on the composite final application. This manufacturing method opens new prospects for the design of thermosetting multifunctional composite materials for a wide variety of applications such as internal damage detection and embedded organic flexible electronics. Highly conductive nanofillers with a proper dispersion and required loadings could be used to tailor the conductivity of resulting nanocomposite for these applications. The internal damage of composite containing conductive fillers could be detected by mapping the electrical conductivity (or impedance) information.

$ F N Q R Z O H G J P H Q W V

The authors acknowledge financial support from FQRNT (Le Fonds Québécois de la Recherche sur la Nature et les Technologies). Prof. El Kahakani acknowledges also the finanial support from NSERC (National Science Engineering Research Council of Canada) and Plasma-Québec (le Réseau Stratégique du FQRNT sur la Science et Technologies des Plasmas). The authors would like to thank the technical support of Dr. Nadir Kchit and Mr. Matthieu Sola for the mechanical characterizations and also Dr. Louis Laberge Lebel and Mr. Charles Tremblay for sample preparation.

5 H I H U H Q F H V

[1] Ear Y, Silverman E. Challenges and opportunities in multifunctional nanocomposite structures for aerospace applications. MRS Bulletin. 2007;32(4):328-34.

[2] Zhou G, Movva S, Lee LJ. Nanoclay and fiber-reinforced composites based on epoxy and phenolic resins. Journal of Applied Polymer Science. 2008;108(6):3720-6.

[3] Bo XZ, Lee CY, Strano MS, Goldfinger M, Nuckolls C, Blanchet GB. Carbon nanotubes-semiconductor networks for organic electronics: The pickup stick transistor. Applied Physics Letters. 2005;86(18):182102, 1-3.

[4] Luo XF, Ou RQ, Eberly DE, Singhal A, Viratyaporn W, Mather PT. A Thermoplastic/Thermoset Blend Exhibiting Thermal Mending and Reversible Adhesion. Acs Applied Materials & Interfaces. 2009;1(3):612-20.

[5] Sgriccia N, Hawley M. Thermal, morphological, and electrical characterization of microwave processed natural fiber composites. Compos Sci Technol. 2007;67(9):1986-91.

[6] Park J, Park S, Lee S. Thermal and mechanical properties of carbon fiber reinforced epoxy composites modified with CTBN and hydroxyl terminated polyester. Adv Polym Emerg Technol 2007:568–72.

[7] Chen W, Shen H, Auad M, Huang C, Nutt S. Basalt fiber–epoxy laminates with functionalized multi-walled carbon nanotubes. Composites: Part A. 2009;40:1082-9.

[8] Huang ZM, Zhang YZ, Kotaki M, Ramakrishna S. A review on polymer nanofibers by electrospinning and their applications in nanocomposites. Composites Science and Technology. 2003;63(15):2223-53.

[9] Chronakis IS. Novel nanocomposites and nanoceramics based on polymer nanofibers using electrospinning process - A review. Journal of Materials Processing Technology. 2005;167(2-3):283-93.

[10] Allaoui A, Bai S, Cheng HM, Bai JB. Mechanical and electrical properties of a MWNT/epoxy composite. Composites Science and Technology. 2002;62(15):1993-8.

[11] Andrews R, Weisenberger MC. Carbon nanotube polymer composites. Current Opinion in Solid State & Materials Science. 2004;8(1):31-7.

[12] Coleman JN, Khan U, Gun'ko YK. Mechanical reinforcement of polymers using carbon nanotubes. Advanced Materials. 2006;18(6):689-706.

[13] Meyyappan M. Carbon nanotubes: science and applications. Boca Raton, Fl: CRC Press; 2005.

[14] Sandler JKW, Kirk JE, Kinloch IA, Shaffer MSP, Windle AH. Ultra-low electrical percolation threshold in carbon-nanotube-epoxy composites. Polymer. 2003;44(19):5893-9.

[15] Moisala A, Li Q, Kinloch IA, Windle AH. Thermal and electrical conductivity of single- and multi-walled carbon nanotube-epoxy composites. Composites Science and Technology. 2006;66(10):1285-8.

[16] Lebel LL, Aissa B, Paez OA, El Khakani MA, Therriault D. Three-dimensional micro structured nanocomposite beams by microfluidic infiltration. Journal of Micromechanics and Microengineering. 2009;19(12):155009, 1-7.

[17] Fan ZH, Advani SG. Characterization of orientation state of carbon nanotubes in shear flow. Polymer. 2005;46(14):5232-40.

[18] Lebel LL, Aissa B, El Khakani MA, Therriault D. Preparation and mechanical characterization of laser ablated single-walled carbon-nanotubes/polyurethane nanocomposite microbeams. Composites Science and Technology. 2010;70(3):518-24.

[19] Thostenson ET, Chou TW. Processing-structure-multi-functional property relationship in carbon nanotube/epoxy composites. Carbon. 2006;44(14):3022-9.

[20] Therriault D, Shepherd RF, White SR, Lewis JA. Fugitive inks for direct-write assembly of three-dimensional microvascular networks. Advanced Materials. 2005;17(4):395-99.

[21] Therriault D, White SR, Lewis JA. Chaotic mixing in three-dimensional microvascular networks fabricated by direct-write assembly. Nature Materials. 2003;2(4):265-71.

[22] Frishfeld V, Lundstrom TS, Jakovics A. Bubble motion through non-crimp fabrics during composites manufacturing. Composites Part A-Applied Science and Manufacturing. 2008;39(2):243-51.

[23] Lundstrom TS. Measurement of void collapse during resin transfer moulding. Composites Part a-Applied Science and Manufacturing. 1997;28(3):201-14.

[24] Nordlund M, Fernberg SP, Lundstrom TS. Particle deposition mechanisms during processing of advanced composite materials. Composites Part a-Applied Science and Manufacturing. 2007;38(10):2182-93.

[25] Advani SG, Chohra M, Yarlagadda S. Filtration of particles through a single layer of dual scale fibrous porous media. Advanced Composites Letters. 2007;16(6):205-21.

[26] Advani SG, Steggall-Murphy C, Simacek P, Barthelemy A, Yarlagadda S, Walsh S. A Model for Particle Deposition during Impregnation of Fibrous Porous Media. Journal of Porous Media. 2011;14(5):383-94.

[27] Hogberg SM, Lundstrom TS. Motion of dispersed carbon nanotubes during impregnation of fabrics. Plastics Rubber and Composites. 2011;40(2):70-9.
[28] Lundstrom TS, Frishfelds V. Modelling of particle deposition during impregnation of dual scale fabrics. Plastics Rubber and Composites. 2011;40(2):65-9.
[29] Lundstrom TS, Gebart BR, Lundemo CY. Void Formation in Rtm. Journal of Reinforced Plastics and Composites. 1993;12(12):1339-49.
[30] Advani SG, Chohra M, Gokce A, Yarlagadda S. Modeling of filtration through multiple layers of dual scale fibrous porous media. Polymer Composites. 2006;27(5):570-81.
[31] Bandow S, Asaka S, Saito Y, Rao AM, Grigorian L, Richter E, et al. Effect of the growth temperature on the diameter distribution and chirality of single-wall carbon nanotubes. Physical Review Letters. 1998;80(17):3779-82.
[32] Wang S, Liang R, Wang B, Zhang C. Reinforcing polymer composites with epoxide-grafted carbon nanotubes. Nanotechnology. 2008;19(8) :085710, 1-7.
[33] Nakashima N, Fujigaya T. Fundamentals and applications of soluble carbon nanotubes. Chemistry Letters. 2007;36(6):692-7.
[34] Gojny FH, Wichmann MHG, Fiedler B, Schulte K. Influence of different carbon nanotubes on the mechanical properties of epoxy matrix composites - A comparative study. Composites Science and Technology. 2005;65(15-16):2300-13.
[35] Barrera EV, Zhu J, Peng HQ, Rodriguez-Macias F, Margrave JL, Khabashesku VN, et al. Reinforcing epoxy polymer composites through covalent integration of functionalized nanotubes. Advanced Functional Materials. 2004;14(7):643-8.
[36] Sun L, Warren GL, O'Reilly JY, Everett WN, Lee SM, Davis D, et al. Mechanical properties of surface-functionalized SWCNT/epoxy composites. Carbon. 2008;46(2):320-8.
[37] Wachtman J. Mechanical properties of ceramics. New York: Wiley; 1996.
[38] Moniruzzaman M, Du FM, Romero N, Winey KI. Increased flexural modulus and strength in SWNT/epoxy composites by a new fabrication method. Polymer. 2006;47(1):293-8.
[39] Wang LF, Zheng QS. Extreme anisotropy of graphite and single-walled carbon nanotube bundles. Applied Physics Letters. 2007;90(15):153113, 1-3.
[40] Carreau PJ, Abbasi S, Derdouri A. Flow induced orientation of multiwalled carbon nanotubes in polycarbonate nanocomposites: Rheology, conductivity and mechanical properties. Polymer. 2010;51(4):922-35.

) L J X U H F D S W L R Q V

) L J X U H Schematic representation of the manufacturing process of a 3D-reinforced nanocomposite beam through micro-infiltration of 3D microfluidic network: (a) deposition of fugitive ink scaffold on an epoxy substrate, (b) encapsulation of the 3D ink-based scaffold using epoxy resin followed by resin solidification, (c) ink removal at 100 °C under vacuum, (d) micro-infiltration of the empty network by the nanocomposite followed by its curing.

) L J X U H (a) Isometric image of a EP2-beam/UVE-infiltrated containing 0.5 wt% SWCNT/UV-epoxy nanocomposite, (b) typical cross-section of a nanocomposite-infiltrated beam, (c)-(e) schematic illustration of the fabricated beams: porous (empty microfluidic network), resin-infiltrated and nanocomposite-infiltrated beams, respectively.

) L J X U H (a) TEM image of the purified SWCNTs soot material which are either in bundles or as individual entities. (b) typical Raman spectrum of the nanotubes featuring three peaks: the radial breathing modes (RBM) at around 185 cm^{-1}, the *-band around 1600 cm^{-1} and the' -band around 1350 cm^{-1}

) L J X U H Optical microscopic image of a 20-µm thick film of SWCNT/UV-epoxy nanocomposites where both submicron and micron-size aggregates are observed.

) L J X U H SEM images of the fracture surface of 3D-reinforced beams in three-point bending test. (a) Typical fracture surface of a representative EP2-beam/UVE-infiltrated and (b) enlarged region on the fiber surface, (c) typical fracture surface of a representative EP2-

beam/NC-UVE-infiltrated and (d) enlarged view on the fiber surface. The dashed lines show the microfibers.

) L J X U H Dynamic mechanical properties of (a) and (b) EP1-beam/UVE-infiltrated and NC-UVE-infiltrated, bulk-UVE and bulk-EP1, (c) and (d) EP2-beam/UVE-infiltrated and NC-UVE-infiltrated, bulk-UVE and bulk-EP2, and (e) and (f) EP1-beam/EP2-infiltrated and NC-EP2-infiltrated, bulk-EP2 and bulk-EP1.

) L J X U H The averaged curves of the flexural stress with respect to the flexural strain for 3D-reinforced beams and bulk-epoxies: (a) bulk-UVE, bulk-EP2 and EP2-beam/UVE-infiltrated and EP2-beam/NC-UVE-infiltrated with the nanocomposite fibers containing two different loading of SWCNT (0.5 wt% and 1wt%) and (b) bulk-EP1, bulk-EP2 and EP1-beam/EP2-infiltrated and EP1-beam/NC-EP2-infiltrated with the nanocomposite fibers containing two different loading of SWCNT (0.5 wt% and 1wt%).

7 D E O H F D S W L R Q V

7 D E O H Different types of 3D-reinforced beams prepared in this study, and their components.

7 D E O H Glass transition temperature (T_g) and storage modulus at 25°C for the 3D-reinforced beams and the bulk epoxies. The variation for the three different types of nanocomposite-infiltrated beams compared to their corresponding neat epoxy-infiltrated beams is presented in the last column.

7 D E O Comparison of increase of storage modulus at 25°C by adding SWCNTs to epoxy matrices achieved in our work with those reported in literature.

7 D E O Flexural properties in the three-point bending test for the 3D-reinforced beams and the bulk epoxies. The variation of the properties for the two different types of nanocomposite-infiltrated beams from their corresponding neat epoxy-infiltrated beams is also presented.

7 D E O Tensile properties of the 3D-reinforced beams and the bulk epoxies. The second and forth columns present the variation of the tensile properties of the two different nanocomposite-infiltrated beams from their corresponding neat epoxy-infiltrated beams. The last column lists the results obtained from rules of mixtures for each type of the infiltrated beams.

) L J X I

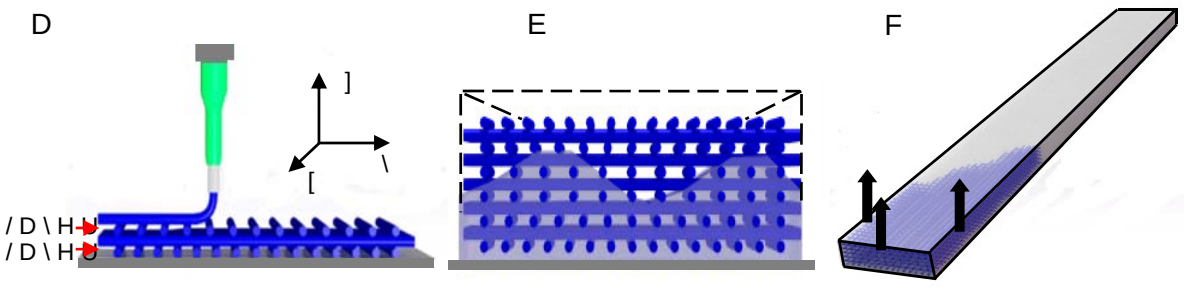
D
E
F
]
[
\
/ D \ H
/ D \ H

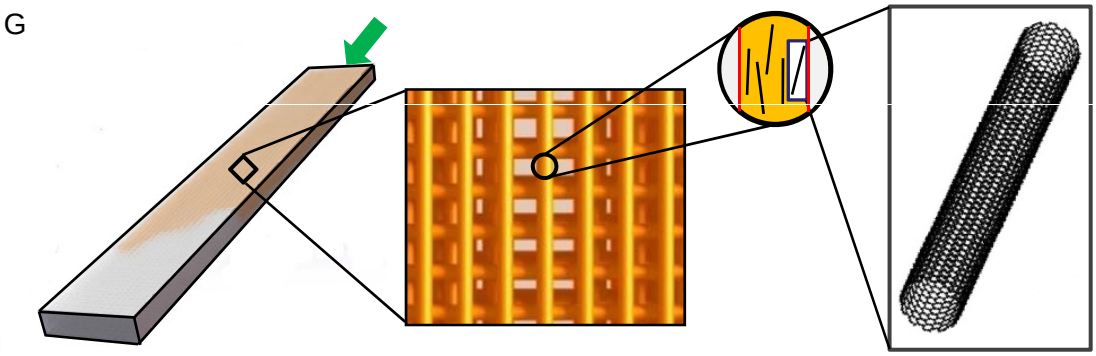
G

) L J X U H

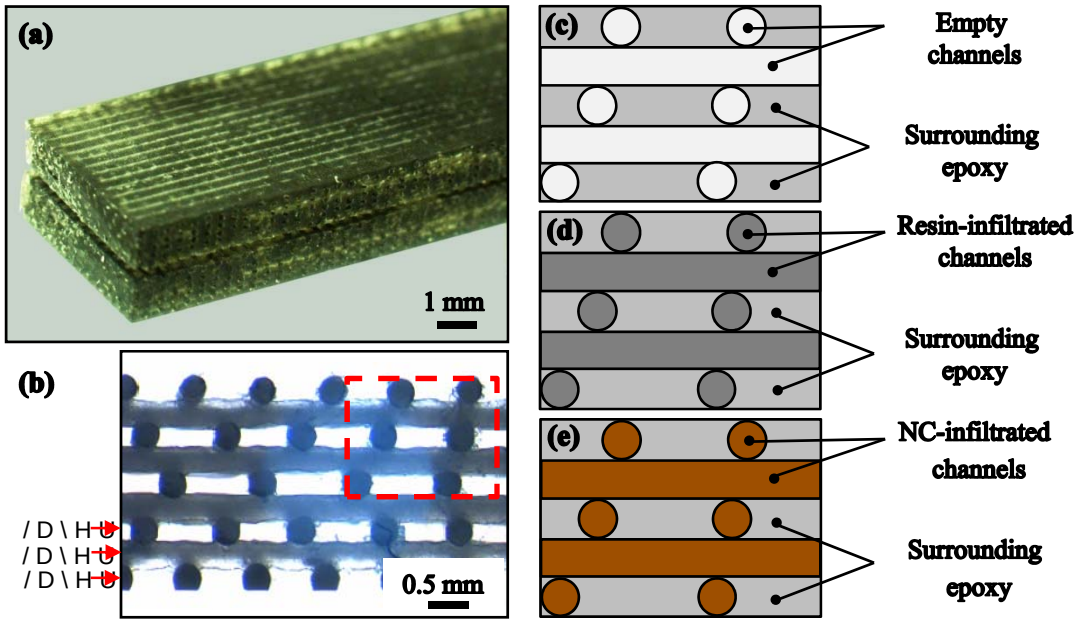
(a)
1 mm
(b)
0.5 mm
/ D \ H
/ D \ H
/ D \ H
(c)
Empty channels
Surrounding epoxy
(d)
Resin-infiltrated channels
Surrounding epoxy
(e)
NC-infiltrated channels
Surrounding epoxy

)LJXUH

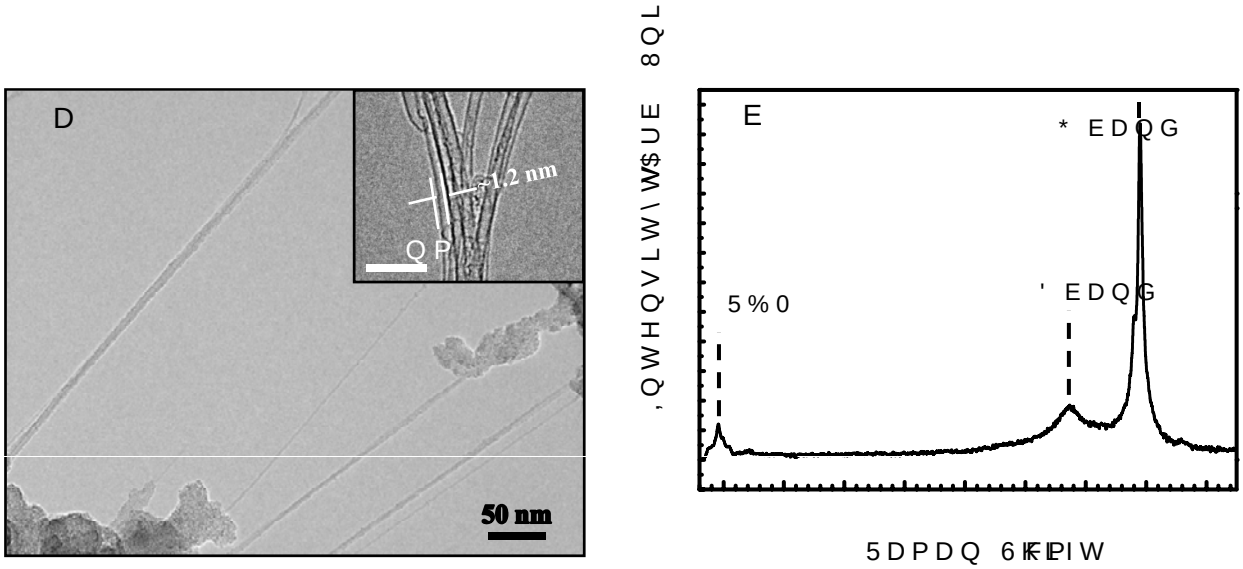

)LJXUH

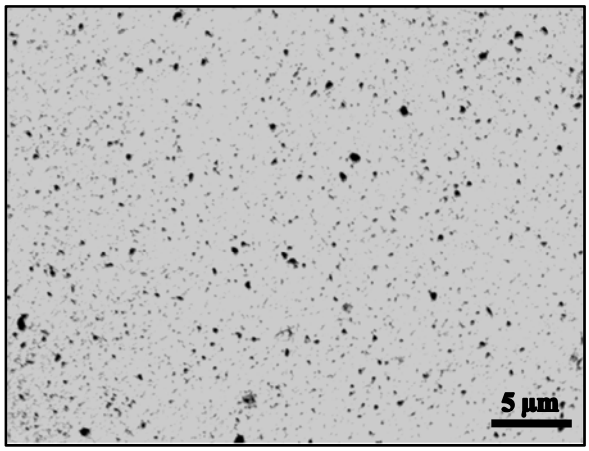

) L J X U H

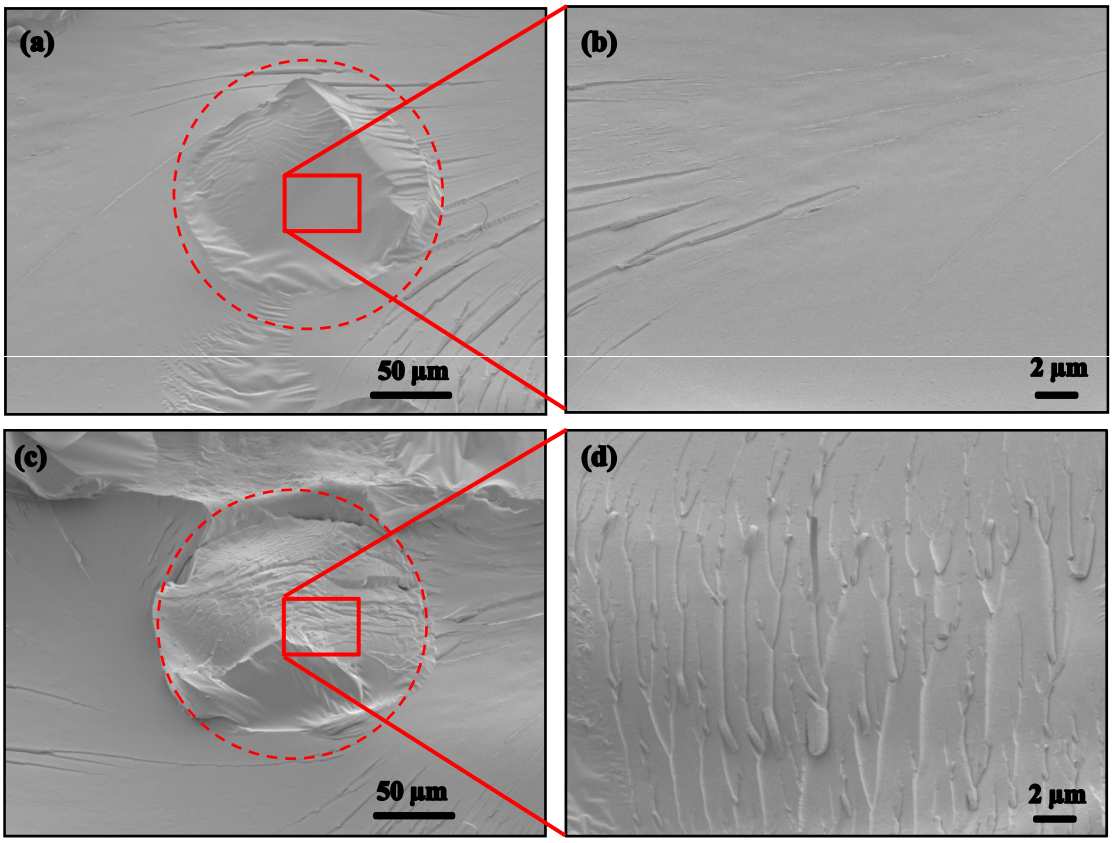

)LJXUH

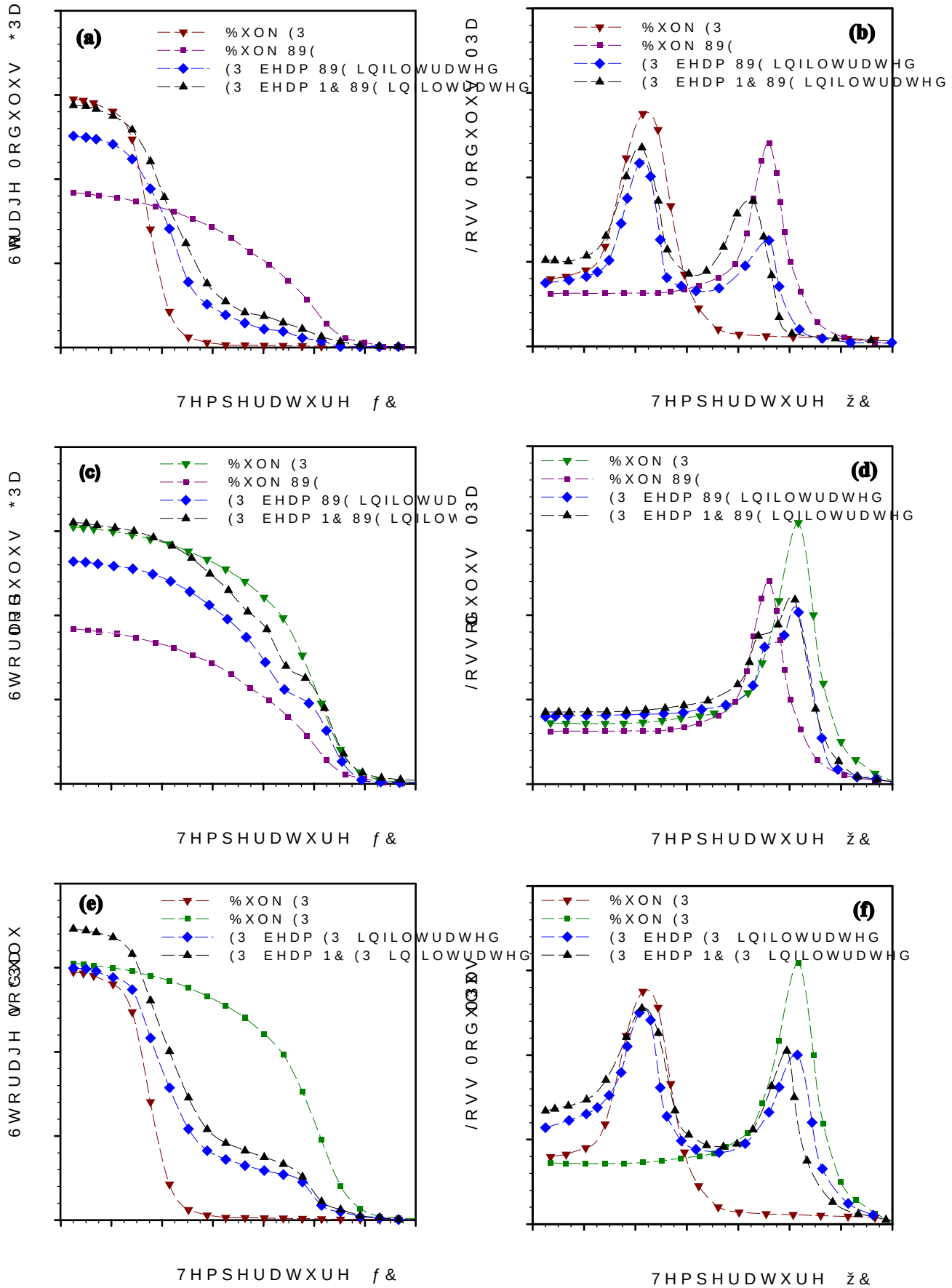
(a)
%XON (3
%XON 89(
(3 EHDP 89(LQILOWUDWHG
(3 EHDP 1& 89(LQ LOWUDWHG
6WUDJH 0RGXOXV *3D
7HPSHUDWXUH f&
(b)
%XON (3
%XON 89(
(3 EHDP 89(LQILOWUDWHG
(3 EHDP 1& 89(LQILOWUDWHG
/RVV 0RGXOXV 03D
7HPSHUDWXUH ž&
(c)
%XON (3
%XON 89(
(3 EHDP 89(LQILOWUD
(3 EHDP 1& 89(LQILOW
6WRUDJH 0RGXOXV *3D
7HPSHUDWXUH f&
(d)
%XON (3
%XON 89(
(3 EHDP 89(LQILOWUDWHG
(3 EHDP 1& 89(LQILOWUDWHG
/RVV 0RGXOXV 03D
7HPSHUDWXUH ž&
(e)
%XON (3
%XON (3
(3 EHDP (3 LQILOWUDWHG
(3 EHDP 1& (3 LQ LOWUDWHG
6WRUDJH 0RGXOXV *3D
7HPSHUDWXUH f&
(f)
%XON (3
%XON (3
(3 EHDP (3 LQILOWUDWHG
(3 EHDP 1& (3 LQILOWUDWHG
/RVV 0RGXOXV 03D
7HPSHUDWXUH ž&

)LJXUH

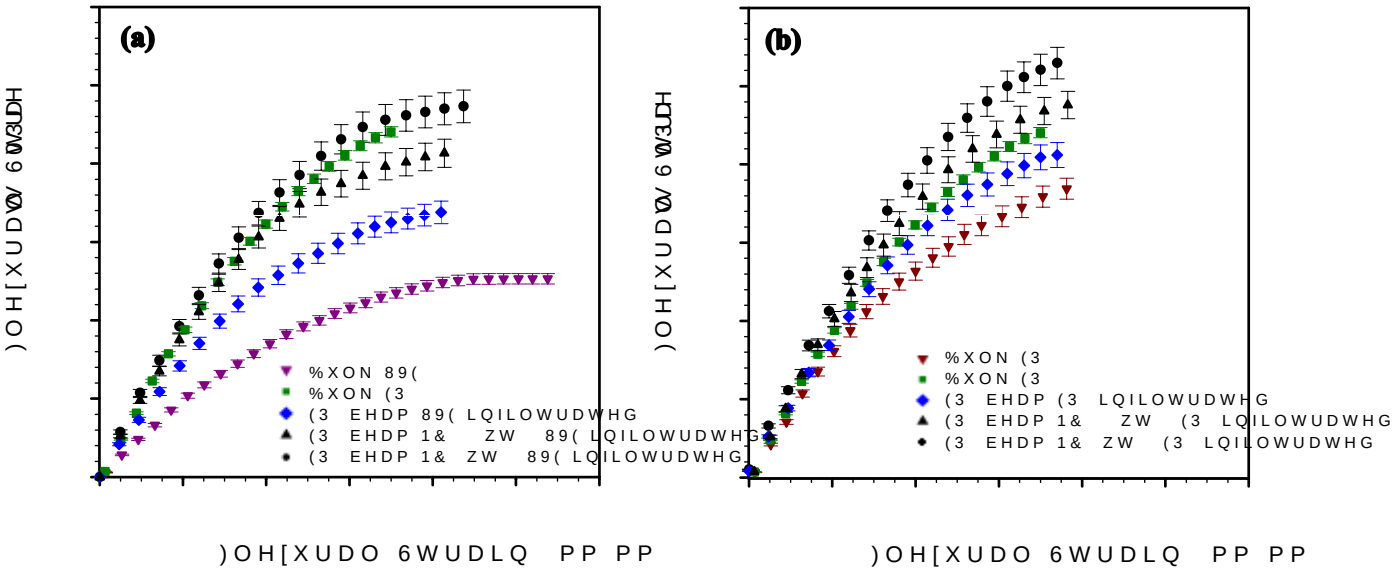
(a)
(b)
%XON 89(
%XON (3
(3 EHDP 89(LQILOWUDWHG
(3 EHDP 1& ZW 89(LQILOWUDWHG
(3 EHDP 1& ZW 89(LQILOWUDWHG
%XON (3
%XON (3
(3 EHDP (3 LQILOWUDWHG
(3 EHDP 1& ZW (3 LQILOWUDWHG
(3 EHDP 1& ZW (3 LQILOWUDWHG
)OH[XUDO 6WUDLQ PP PP
)OH[XUDO 6WUDLQ PP PP

7 D E O H

Type of sample		Components	
		Matrix (material-surrounded)	Microfiber (material-infiltrated)
Resin-infiltrated beams	EP1-beam/UVE-infiltrated	EPON 828	UV-epoxy
	EP2-beam/UVE-infiltrated	EPON 862	UV-epoxy
	EP1-beam/EP2-infiltrated	EPON 828	EPON 862
Nanocomposite-infiltrated beams	EP1-beam/NC-UVE-infiltrated	EPON 828	UV-epoxy/SWCNT nanocomposite
	EP2-beam/NC-UVE-infiltrated	EPON 862	UV-epoxy/SWCNT nanocomposite
	EP1-beam/NC-EP2-infiltrated	EPON 828	EPON 862/SWCNT nanocomposite

7 D E O H

Type of sample	Glass transition temperature, 7_J (°C)	Storage modulus at 25°C (GPa)	Storage modulus at 25°C Var. (%)
Bulk-UVE	~115	1.84	---
Bulk-EP1	~60	2.95	---
Bulk-EP2	~125	3.05	---
EP1-beam/UVE-infiltrated	~60 and ~115	2.51	0
EP1-beam/NC-UVE-infiltrated	~60 and ~110	2.88	15
EP2-beam/UVE-infiltrated	~125 and ~115	2.64	0
EP2-beam/NC-UVE-infiltrated	~125 and ~109	3.11	18
EP1-beam/EP2-infiltrated	~60 and ~125	2.99	0
EP1-beam/NC-EP2-infiltrated	~60 and ~121	3.46	16

7 D E O H

Researcher		SWCNTs wt.%	Increase of Storage Modulus at 25°C (%)	Normalized (Increase of Storage Modulus/wt.%) (%)
Barrera et al. [35]		1.0	44	44
Sun et al. [32]		1.0	20	20
Wang et al. [36]		1.0	41	41
Our results	EP1-beam/NC-UVE-infiltrated	0.18 (in whole beam)	15	83
	EP2-beam/NC-UVE-infiltrated	0.18 (in whole beam)	17	94
	EP1-beam/NC-EP2-infiltrated	0.18 (in whole beam)	16	88

7 D E O H

Type of sample	Flexural modulus (GPa)	Flexural modulus Var. (%)	Flexural strength (MPa)	Flexural strength Var. (%)
Bulk UVE	1.63	---	50.6	---
Bulk EP1	2.54	---	73.8	---
Bulk EP2	3.15	---	88.1	---
EP2-beam/UVE-infiltrated	2.41	0	69.8	0
EP2-beam/NC(0.5wt%)-UVE-infiltrated	3.06	+27	82.2	+18
EP2-beam/NC(1wt%)-UVE-infiltrated	3.36	+39	92.1	+31
EP1-beam/EP2-infiltrated	2.82	0	82.4	0
EP1-beam/NC(0.5wt%)-EP2-infiltrated	3.43	+22	95.2	+16
EP1-beam/NC(1wt%)-EP2-infiltrated	3.78	+34	105.2	+28

7 D E O H

Type of sample	Tensile Strength (MPa)	Tensile Strength Var. (%)	Young's Modulus (GPa)	Young's Modulus Var. (%)	Young's Modulus-Rules of Mixtures (GPa)
Bulk UVE	50.4	---	1.32	---	---
Bulk EP1	71.3	---	2.83	---	---
Bulk EP2	79.8	---	3.10	---	---
EP2-beam/UVE-infiltrated	64.7	0	2.34	0	2.47
EP2-beam/NC(0.5wt%)-UVE-infiltrated	68.9	+7	2.64	+11	2.83
EP2-beam/NC(1wt%)-UVE-infiltrated	72.4	+12	2.82	+17	3.13
EP1-beam/EP2-infiltrated	74.3	0	2.81	0	2.92
EP1-beam/NC(0.5wt%)-EP2-infiltrated	78.8	+6	3.06	+9	3.28
EP1-beam/NC(1wt%)-EP2-infiltrated	81.7	+10	3.26	+16	3.58

)LJXUH

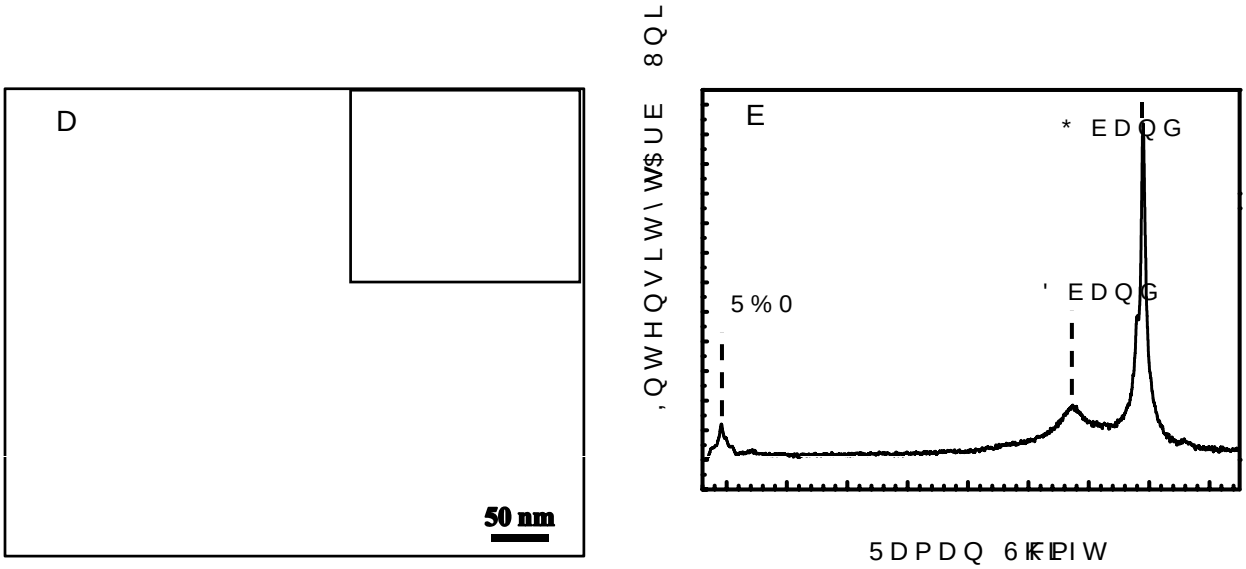

)LJXUH